

Imaging two-dimensional generalized Wigner crystals

<https://doi.org/10.1038/s41586-021-03874-9>

Received: 3 April 2021

Accepted: 4 August 2021

Published online: 29 September 2021

 Check for updates

Hongyuan Li^{1,2,3,9}, Shaowei Li^{1,3,4,5,9}✉, Emma C. Regan^{1,2,3}, Danqing Wang^{1,2}, Wenyu Zhao¹, Salman Kahn^{1,3}, Kentaro Yumigeta⁶, Mark Blei⁶, Takashi Taniguchi⁷, Kenji Watanabe⁸, Sefaattin Tongay⁶, Alex Zettl^{1,3,4}, Michael F. Crommie^{1,3,4}✉ & Feng Wang^{1,3,4}✉

The Wigner crystal¹ has fascinated condensed matter physicists for nearly 90 years^{2–14}. Signatures of two-dimensional (2D) Wigner crystals were first observed in 2D electron gases under high magnetic field^{2–4}, and recently reported in transition metal dichalcogenide moiré superlattices^{6–9}. Direct observation of the 2D Wigner crystal lattice in real space, however, has remained an outstanding challenge. Conventional scanning tunnelling microscopy (STM) has sufficient spatial resolution but induces perturbations that can potentially alter this fragile state. Here we demonstrate real-space imaging of 2D Wigner crystals in WSe₂/WS₂ moiré heterostructures using a specially designed non-invasive STM spectroscopy technique. This employs a graphene sensing layer held close to the WSe₂/WS₂ moiré superlattice. Local STM tunnel current into the graphene layer is modulated by the underlying Wigner crystal electron lattice in the WSe₂/WS₂ heterostructure. Different Wigner crystal lattice configurations at fractional electron fillings of $n = 1/3, 1/2$ and $2/3$, where n is the electron number per site, are directly visualized. The $n = 1/3$ and $n = 2/3$ Wigner crystals exhibit triangular and honeycomb lattices, respectively, to minimize nearest-neighbour occupations. The $n = 1/2$ state spontaneously breaks the original C3 symmetry and forms a stripe phase. Our study lays a solid foundation for understanding Wigner crystal states in WSe₂/WS₂ moiré heterostructures and provides an approach that is generally applicable for imaging novel correlated electron lattices in other systems.

A Wigner crystal is the crystalline phase of electrons stabilized at low electron density where long-range Coulomb interactions dominate over quantum fluctuations in electron motion. The long pursuit of Wigner crystals^{2–10} has motivated the study of two-dimensional (2D) electron gases at high magnetic field where electron kinetic energy is quenched by degenerate Landau levels^{15,16} and has led to the discovery of new quantum hall states^{17,18}. Electrical transport signatures of Wigner crystal states have been reported in extremely clean GaAs/AlGaAs quantum wells^{2,3} as well as graphene⁴ at sufficiently low doping and high magnetic field. Signs of Wigner crystallization have also been detected for electrons trapped at the surface of liquid helium^{11–14}. Recently, the discovery of moiré flat minibands in van der Waals heterostructures has opened a new route to realize Wigner crystal states at zero magnetic field¹⁹. Several optical and conductance measurements have provided evidence of rich generalized Wigner crystal states (generalized on a lattice background²⁰) in different transition metal dichalcogenide (TMDC) moiré superlattices^{6–9}. This evidence for 2D Wigner crystals, in the form of new transport and optical responses at fractional charge filling factors, is indirect and could potentially

be explained by other quantum phases such as fractional quantum Hall states¹⁷. The most direct evidence of 2D Wigner crystals would be real-space imaging of the 2D electron lattice, which has remained an outstanding experimental challenge.

Real-space imaging of 2D Wigner crystals places stringent requirements on the measurement technique. It must simultaneously have high spatial resolution, high single-electron sensitivity, and low perturbation to the electron lattice. The last two requirements conflict with each other since high sensitivity requires strong coupling to the Wigner crystal whereas a low perturbation requires weak coupling. For example, conventional scanning tunnelling microscopy (STM) measurements have excellent spatial resolution and charge sensitivity but can be highly invasive since inevitable tip-gating effects can destroy the delicate Wigner crystal lattice. Here we utilize a novel STM measurement scheme that strikes a balance between these two competing requirements, thus enabling real-space imaging of the $n = 2/3, n = 1/2$ and $n = 1/3$ 2D Wigner crystal states in WSe₂/WS₂ moiré heterostructures.

Our new STM scheme employs a specially designed van der Waals heterostructure, as illustrated in Fig. 1a (see Methods for the sample

¹Department of Physics, University of California at Berkeley, Berkeley, CA, USA. ²Graduate Group in Applied Science and Technology, University of California at Berkeley, Berkeley, CA, USA.

³Materials Sciences Division, Lawrence Berkeley National Laboratory, Berkeley, CA, USA. ⁴Kavli Energy Nano Sciences Institute at the University of California Berkeley and the Lawrence Berkeley National Laboratory, Berkeley, CA, USA. ⁵Department of Chemistry and Biochemistry, University of California at San Diego, La Jolla, CA, USA. ⁶School for Engineering of Matter, Transport and Energy, Arizona State University, Tempe, AZ, USA. ⁷International Center for Materials Nanoarchitectonics, National Institute for Materials Science, Tsukuba, Japan. ⁸Research Center for Functional Materials, National Institute for Materials Science, Tsukuba, Japan. ⁹These authors contributed equally: Hongyuan Li, Shaowei Li. [✉]e-mail: shaoweli@ucsd.edu; crommie@berkeley.edu; fengwang76@berkeley.edu

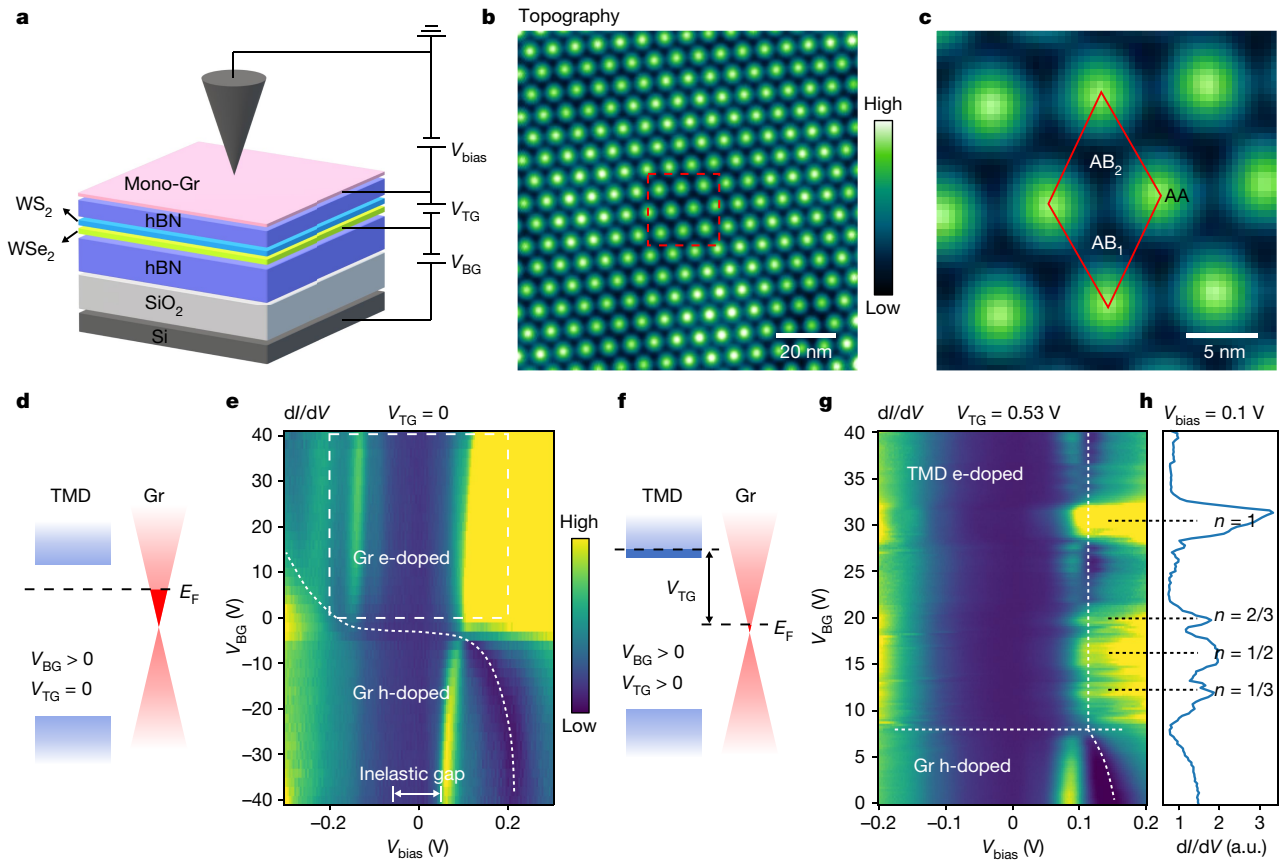


Fig. 1 | STM measurement of Wigner crystal states in a dual-gated WSe₂/WS₂ moiré superlattice. **a**, Schematic of the dual-gated WSe₂/WS₂ moiré heterostructure device. The top hBN thickness (5 nm) is slightly smaller than the moiré lattice constant (8 nm). Top gate (V_{TG}) and bottom gate (V_{BG}) voltages are applied to separately control the carrier density in the WSe₂/WS₂ heterostructure as well as the top graphene sensing layer. **b**, A typical large-scale topography image measured on the top graphene surface. $V_{bias} = 180$ mV and $I = 300$ pA. **c**, Magnified image of the red dashed box in **b**. The red rhombus labels a primitive cell. Peaks correspond to AA stacking regions and the two inequivalent low points correspond to distinct AB stacking regions (denoted AB₁ and AB₂). **d**, Schematic of the heterostructure band alignment and Fermi levels for $V_{TG} = 0$ and $V_{BG} > 0$. At zero V_{TG} , the Fermi level of the WSe₂/WS₂ heterostructure is located in the bandgap. **e**, V_{BG} -dependent dI/dV spectra measured on the graphene sensing layer over an AA stacking site for $V_{TG} = 0$. The dispersive feature marked by the white dotted curve shows the evolution of the graphene charge neutral point (CNP) induced by electrostatic doping from V_{BG} . The persistent gap near $V_{bias} = 0$ arises from an inelastic tunnelling gap that

exists at all gate voltages. Due to this inelastic tunnelling gap, the graphene CNP curve shows an abrupt shift as it shifts over the zero-bias region. The tip height was set by the following parameters: $V_{bias} = -300$ mV and $I = 100$ pA. **f**, Schematic of the heterostructure band alignment and Fermi levels for $V_{TG} > 0$ and $V_{BG} > 0$. Application of an appropriate positive V_{TG} allows the Fermi level of the WSe₂/WS₂ heterostructure to be lifted into the conduction band. **g**, V_{BG} -dependent dI/dV spectra measured on the graphene sensing layer over an AA stacking site for $V_{TG} = 0.53$ V. This is a magnification of the electron-doped regime corresponding to the phase space denoted by the white dashed box in **e**. The graphene is hole-doped in the region below the horizontal dashed line ($V_{BG} < 7$ V), and the WSe₂/WS₂ is electron-doped in the region above it ($V_{BG} > 7$ V). The vertical white dash curve indicates the expected movement of the graphene CNP for a non-interacting picture. Notable electron doping of the graphene layer takes place at $n = 1/3, 1/2, 2/3$ and 1 (denoted by horizontal black dashed lines in **g**). The tip height was set by the following parameters: $V_{bias} = -200$ mV and $I = 100$ pA. **h**, Vertical line-cut through the V_{BG} -dependent dI/dV spectra in **g** at $V_{bias} = 0.1$ V shows peaks at $n = 1, 2/3, 1/2$ and $1/3$.

fabrication details). It integrates a gated WSe₂/WS₂ moiré heterostructure and a top graphene monolayer sensing layer that are separated by a hexagonal boron nitride (hBN) layer with a thickness $d_t = 5$ nm. This separation is small enough that the STM tip and graphene layer can efficiently couple to individual moiré electrons in the WSe₂/WS₂ superlattice (moiré lattice constant ~8 nm), but still large enough that the tip and graphene layer remain non-invasive with respect to the delicate Wigner crystal states. STM tunnelling current into the graphene sensing layer can be modulated by the charge states of different moiré sites in the WSe₂/WS₂ superlattice through local Coulomb blockade effects²¹. This technique allows us to detect the local charge distribution in the WSe₂/WS₂ heterostructure and to image the embedded Wigner crystal lattice.

Figure 1b shows a typical large-scale topography image measured on the top graphene surface. The top graphene and hBN layers cover the WSe₂/WS₂ heterostructure conformally and inherit the topography of the three-dimensional (3D) reconstructed moiré superlattice²² below.

Figure 1c shows a magnified topographic image corresponding to the red dashed box area in Fig. 1b. A red rhombus labels the primitive cell of the moiré superlattice with the four high points corresponding to AA stacking regions and the two inequivalent low points corresponding to distinct AB stacking regions (denoted AB₁ and AB₂)²². The measured moiré lattice constant is $L_M = 8$ nm, yielding a near 0° twist angle (see Methods for details).

The WSe₂/WS₂ heterostructure is dual-gated by the top graphene sensing layer (top gate) and the silicon substrate (back gate) (Fig. 1a). The top gate dielectric is defined by the top hBN flake ($d_t = 5$ nm) while the bottom gate dielectric is defined by a combination of SiO₂ ($d_{SiO_2} = 285$ nm) and hBN ($d_b = 70$ nm). The carrier densities in the WSe₂/WS₂ heterostructure and the top graphene can be controlled independently via the top gate voltage, V_{TG} , and bottom gate voltage, V_{BG} . In this study we mainly focus on the electron-doped regime of the WSe₂/WS₂ heterostructure.

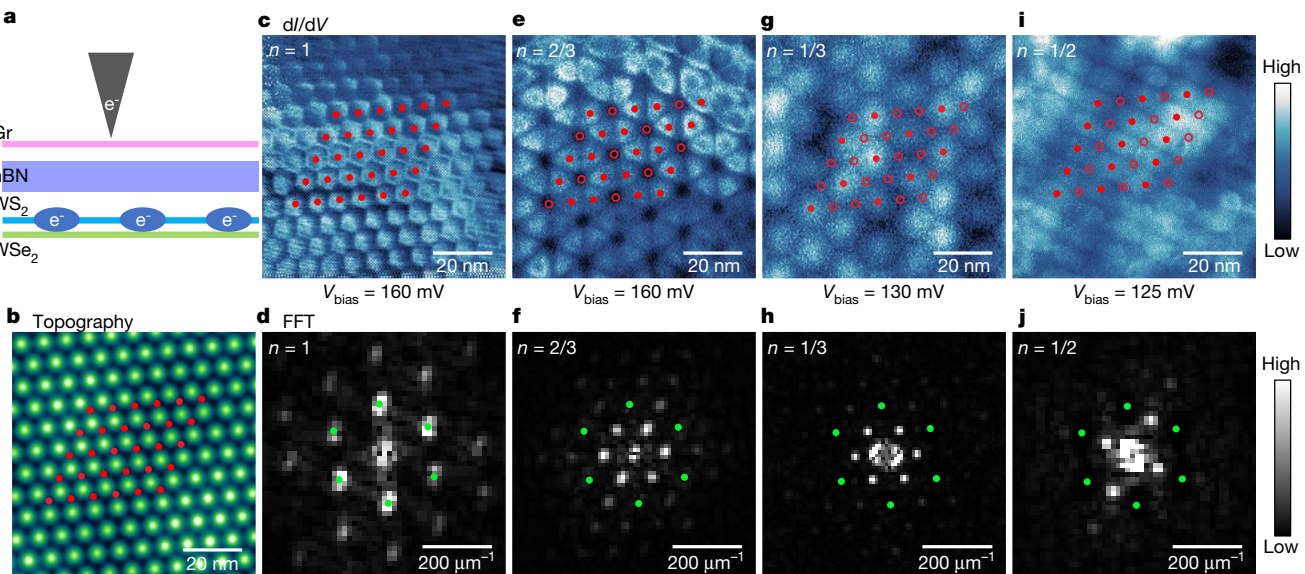


Fig. 2 | Imaging Mott and generalized Wigner crystal states. **a**, Schematic shows imaging of correlated states in a WSe₂/WS₂ moiré superlattice beneath a graphene sensing layer. d/dV maps are acquired at the top graphene surface. **b**, A typical STM topographic image of the moiré superlattice shows a perfect lattice without distortion or defects. The triangular lattice formed by the AB₁ stacking sites is marked by solid red dots. **c**, d/dV map of the $n = 1$ Mott insulator ($V_{\text{bias}} = 160$ mV, $V_{\text{BG}} = 30$ V, $V_{\text{TG}} = 0.53$ V). The triangular lattice formed by the AB₁ stacking sites is labelled with red dots. **d**, Fast Fourier transform (FFT) of the image shown in **c**. The reciprocal unit vectors of the moiré superlattice are labelled by green dots. **e–j**, d/dV maps of the generalized Wigner crystal states for different electron fillings and their corresponding

FFT images: **e**, d/dV map of $n = 2/3$ state ($V_{\text{bias}} = 160$ mV, $V_{\text{BG}} = 21.8$ V, $V_{\text{TG}} = 0.458$ V). **f**, FFT of $n = 2/3$ state shown in **e**. **g**, d/dV map of $n = 1/3$ state ($V_{\text{bias}} = 130$ mV, $V_{\text{BG}} = 14.9$ V, $V_{\text{TG}} = 0.458$ V). **h**, FFT of $n = 1/3$ state shown in **g**. **i**, d/dV map of $n = 1/2$ state ($V_{\text{bias}} = 125$ mV, $V_{\text{BG}} = 18.7$ V, $V_{\text{TG}} = 0.458$ V). **j**, FFT of $n = 1/2$ state shown in **i**. FFT filtering was performed in the Wigner crystal images (**e–j**) to suppress the periodic features associated with the moiré superlattice (that is, green dots in **f**, **h** and **j**; see Extended Data Fig. 3 for unfiltered images). Electron-filled AB₁ sites are labelled with solid red dots and the empty AB₁ sites are labelled with open red circles in the real-space images (**e**, **g**, **i**). The locations of the reciprocal unit vectors of the moiré superlattice are marked by green dots in (**f**, **h**, **j**).

For $V_{\text{TG}} = 0$, the Fermi level is within the band gap for the WSe₂/WS₂ heterostructure (see illustration in Fig. 1d). In this case, tuning V_{BG} dopes charge carriers exclusively into the graphene layer. Figure 1e shows a 2D plot of the STM differential conductivity (d/dV) spectra of graphene at $V_{\text{TG}} = 0$ for different values of V_{BG} (see Methods for individual d/dV spectra at different gate voltages). The dispersive feature labelled by the white dashed line shows the evolution of the graphene charge neutral point (CNP) in response to the electrostatic doping from V_{BG} (refs. ^{23–25}). The persistent gap near $V_{\text{bias}} = 0$ arises from an inelastic tunnelling gap that occurs at all gate voltages and causes the graphene CNP curve to abruptly shift as it ramps through the zero-bias region^{23,25}.

We can dope electrons into the WSe₂/WS₂ heterostructure by applying a positive V_{TG} such that the WSe₂/WS₂ heterostructure Fermi level lies near the conduction band edge (see illustration in Fig. 1f). Here we choose $V_{\text{TG}} \approx 0.5$ V so that the WSe₂/WS₂ heterostructure can be electron-doped while the graphene sensing layer remains close to charge neutral. The reason for doing this is that the resulting small density of states for graphene provides the highest sensitivity for imaging Wigner crystal states in the moiré superlattice. Charge neutral graphene also has less of a screening effect on the moiré electron–electron interactions due to the long screening length of Dirac electrons at the CNP²⁶. Figure 1g shows the resulting d/dV spectra as a function of V_{BG} at a fixed $V_{\text{TG}} = 0.53$ V. This panel corresponds to the same $\{V_{\text{BG}}, V_{\text{bias}}\}$ phase space outlined by the dashed white box in Fig. 1e, but for non-zero V_{TG} .

Figure 1g shows that the graphene is hole-doped at $V_{\text{BG}} < 7$ V, while the WSe₂/WS₂ heterostructure cannot be hole-doped under these conditions given the band alignment shown in Fig. 1f. The graphene hole doping leads to dispersive movement of the graphene CNP at $V_{\text{BG}} < 7$ V (denoted by the white dashed line in Fig. 1g). Electron doping for $V_{\text{BG}} > 7$ V, however, leads to very different behaviour. In a non-interacting single-particle picture, the electron doping would

occur predominantly in the WSe₂/WS₂ heterostructure because its density of states (DOS) is orders of magnitude larger than the graphene DOS at the Dirac point. Therefore, one would expect the graphene Fermi energy to stay fixed near the Dirac point, as illustrated by the vertical dashed line at $V_{\text{BG}} > 7$ V. Experimentally, however, we observe a non-trivial shift of the graphene CNP with respect to the Fermi energy at different V_{BG} values. The graphene layer undergoes electron doping when the WSe₂/WS₂ heterostructure experiences fractional filling of the moiré superlattice with $n = 1/3, 1/2, 2/3$ and 1 (black dashed lines in Fig. 1g). Figure 1h displays a vertical line-cut of the gate-dependent d/dV spectra at $V_{\text{bias}} = 0.1$ V, showing clear peaks at these fractional fillings. These features signify the correlated gaps in the WSe₂/WS₂ Mott insulator state at $n = 1$ as well as the generalized Wigner crystal insulator states at $n = 1/3, 1/2, 2/3$. This is because the correlated gaps make the WSe₂/WS₂ heterostructure electronically incompressible and so electrons are electrostatically forced into the graphene sensing layer. Similar effects have been observed for capacitance and single-electron-transistor measurements of electronic compressibility in different van der Waals heterostructure systems^{27–31}. Our STM configuration thus provides a new technique for mapping the local electronic compressibility of correlated insulating states in moiré superlattices.

Real-space imaging of the 2D electron lattice of the Mott insulator and Wigner crystal states was performed through 2D d/dV mapping of the graphene sensing layer, as illustrated in Fig. 2a. The Mott and Wigner crystal states form periodic electron lattices in the WSe₂/WS₂ moiré heterostructure that couple to the graphene sensing layer and STM tip through long-range Coulomb interactions. The tunnel current between the STM tip and the graphene layer will vary spatially depending on the charge state of the WSe₂/WS₂ moiré site below the STM tip. As a result, the electron lattices of the Mott and Wigner crystal states

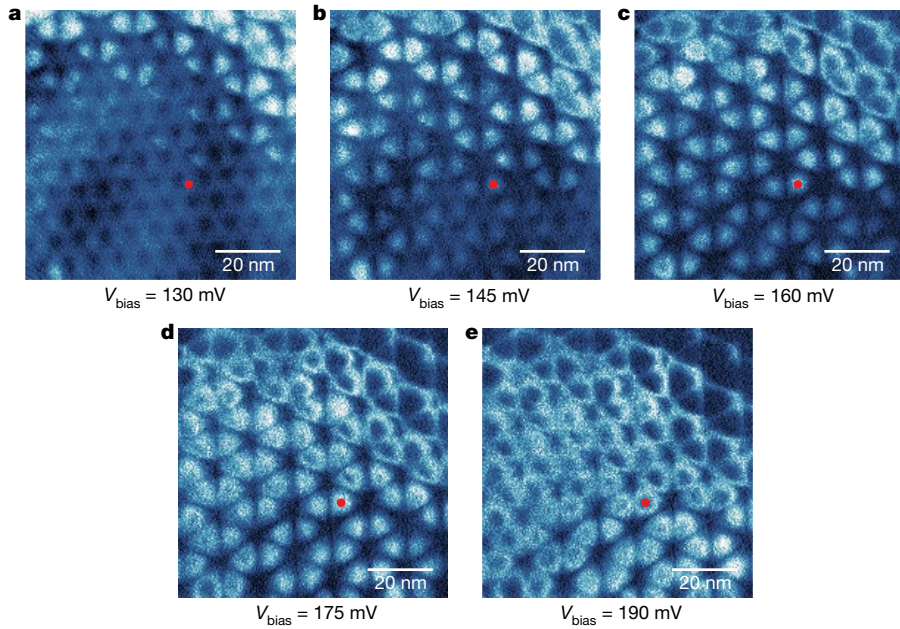


Fig. 3 | Evolution of dI/dV maps for the $n = 2/3$ state with increased V_{bias} . **a–e**, dI/dV maps of the $n = 2/3$ generalized Wigner crystal state measured for $V_{\text{bias}} = 130$ mV (a), $V_{\text{bias}} = 145$ mV (b), $V_{\text{bias}} = 160$ mV (c), $V_{\text{bias}} = 175$ mV (d) and $V_{\text{bias}} = 190$ mV (e). Gate voltage parameters: $V_{\text{BG}} = 21.8$ V, $V_{\text{TG}} = 0.458$ V. All five maps are measured in the same region and no filtering has been performed.

The map in c ($V_{\text{bias}} = 160$ mV) shows the same data as Fig. 2e, but with no filtering. The red dot labels one typical electron-filled AB_1 site where a discharging ring can be observed that gets larger with increased V_{bias} (a common characteristic of discharging phenomena).

can be imaged as periodic lattice structures in 2D dI/dV mappings of the graphene sensing layer.

Figure 2b displays the topographic image of a typical region of the WSe_2/WS_2 moiré superlattice. The triangular lattice formed by the AB_1 stacking sites have been marked with solid red dots. This region exhibits a lattice that is free of distortion or atomic defects, an essential condition for observing Mott and Wigner crystal states with long-range order.

Figure 2c shows a dI/dV mapping of the graphene layer when the WSe_2/WS_2 moiré heterostructure is in the $n = 1$ Mott insulator state ($V_{\text{bias}} = 160$ mV, $V_{\text{BG}} = 30$ V and $V_{\text{TG}} = 0.53$ V; see Methods for more measurement details). A highly ordered triangular lattice of bright features can be clearly observed that corresponds to the AB_1 stacking sites of the moiré superlattice. Such AB_1 stacking sites are illustrated as red dots in Fig. 2b. Since the AB_1 and AB_2 stackings sites are similar in topography, the centring of the bright features in Fig. 1c on the AB_1 stacking sites implies that these features do not originate from topography, but rather from the underlying electron lattice of the Mott insulator state. This is consistent with previous work showing that conduction flat band electrons in the WSe_2/WS_2 moiré heterostructure are localized at one of the AB stacking sites²¹. Figure 2d displays the fast Fourier transform (FFT) image of the dI/dV map in Fig. 2c, showing sharp diffraction points associated with the electron lattice of the Mott insulator state. The reciprocal unit vectors of the moiré superlattice are marked by green dots in the FFT image and are seen to overlap perfectly with the lowest order diffraction points of the Mott insulator electron lattice.

We next imaged the generalized Wigner crystal states at fractional fillings. Figure 2e shows the dI/dV mapping of the $n = 2/3$ generalized Wigner crystal state ($V_{\text{bias}} = 160$ mV, $V_{\text{BG}} = 21.8$ V and $V_{\text{TG}} = 0.458$ V). FFT filtering has been performed on this and subsequent Wigner crystal images in Fig. 2 to suppress periodic features associated with the moiré superlattice (that is, the green dots in Fig. 2f; see Methods for unfiltered images). The $n = 2/3$ dI/dV map exhibits a honeycomb lattice with lattice constant $\sqrt{3}L_M$. This is consistent with 2/3 of the available AB_1 sites being filled with electrons (that is, the solid red dots located in bright regions of the image) and the other 1/3 AB_1 sites being empty (that is, the open red circles located in dark regions of the image) so as to

minimize total nearest-neighbour interactions. Such a honeycomb lattice matches previous predictions^{6–9} and confirms the existence of generalized Wigner crystal states where moiré electrons are stabilized by long-range Coulomb interactions and exhibit well-defined 2D crystalline order. The corresponding FFT image (Fig. 2f) demonstrates the emergence of a new lattice: six sharp diffraction points associated with the generalized Wigner crystal lattice appear inside the reciprocal unit vectors (green dots) of the moiré superlattice.

Figure 2g, h shows the dI/dV map and corresponding FFT image, respectively, of the $n = 1/3$ generalized Wigner crystal state ($V_{\text{bias}} = 130$ mV, $V_{\text{BG}} = 14.9$ V and $V_{\text{TG}} = 0.458$ V). The real-space image demonstrates a new triangular electron lattice associated with a Wigner crystal state where 1/3 of the available AB_1 sites are filled with electrons (solid red dots) and the other 2/3 AB_1 sites are empty (open red circles). The FFT image shows a clear diffraction pattern of the generalized Wigner crystal state with a lattice constant of $\sqrt{3}L_M$. The $n = 2/3$ and $n = 1/3$ states have similar diffraction patterns since they share the same primitive cell and are linked by a particle–hole transformation.

Figure 2i shows a dI/dV map of the $n = 1/2$ generalized Wigner crystal state ($V_{\text{bias}} = 125$ mV, $V_{\text{BG}} = 18.7$ V and $V_{\text{TG}} = 0.458$ V). The image reveals unambiguously that the C3 symmetry of the host moiré superlattice is spontaneously broken for this generalized Wigner crystal state. The $n = 1/2$ state features a stripe symmetry with electrons (solid red dots) filling the AB_1 sites in alternating lines (empty sites are marked by open red circles). The lattice constants of this stripe phase are L_M and $\sqrt{3}L_M$ along the parallel and perpendicular directions, respectively. The corresponding FFT image in Fig. 2j shows rhombus-like reciprocal unit vectors, further confirming the broken symmetry of this stripe phase for the $n = 1/2$ generalized Wigner crystal state.

The $n = 1/2$ generalized Wigner crystal state is predicted to be highly degenerate, with multiple electron lattice configurations having the same energy in the case of only nearest-neighbour interactions⁷. The spontaneous broken symmetry of the $n = 1/2$ state might therefore be governed by higher-order effects, such as next-nearest-neighbour interactions and/or accidental strain in the lattice (uniaxial strain ~0.39%). We have also noticed that the $n = 1/2$ electron lattice is more fragile than

the $n = 1/3$ and $2/3$ states. More discussion on the broken symmetry and fragility of the $n = 1/2$ states is included in the Methods.

We last discuss the imaging mechanism underlying the dI/dV mapping of generalized Wigner crystal lattices assisted by a graphene sensing layer. As illustrated in Fig. 2a, the STM tunnelling current into the graphene layer can be coupled to moiré electrons below the tip through long-range Coulomb interactions. This coupling can affect the tunnel current in two different ways: (1) the localized moiré electrons can induce local band bending in the graphene sensing layer, thus changing the graphene local density of states and hence the dI/dV signal; (2) application of V_{bias} can discharge the moiré electron right below the tip once V_{bias} exceeds a threshold value. This mechanism is helped by the fact that electrical screening by the top monolayer graphene is weak when its Fermi level is close to the Dirac point. A resulting moiré electron discharging event could then lead to a sudden increase in the STM tunnelling current due to the elimination of the Coulomb blockade effect, hence contributing to a stronger dI/dV signal²¹.

To distinguish between these two mechanisms, we systematically examined the dI/dV map evolution with changing V_{bias} . Figure 3a–e shows dI/dV maps of the $n = 2/3$ Wigner crystal state as V_{bias} is increased from 130 mV to 190 mV. No FFT filtering was performed on these images. The honeycomb lattice associated with the $n = 2/3$ state is not so clearly seen at $V_{\text{bias}} = 130$ mV (Fig. 3a) but emerges when V_{bias} is increased to 145 mV (Fig. 3b). The dominant features are the bright dots centred on the AB_1 stacking sites. These features expand with increased V_{bias} (Fig. 3c) and ultimately form ring-like features (Fig. 3d, e). Such behaviour (that is, expanding rings with increased tip bias) is characteristic of tip-induced electrical discharging rings^{21,32–35} and occurs because electrical discharging for larger tip–electron distances requires larger tip biases. This indicates that mechanism (2) discussed above is the dominant contrast mechanism for imaging Wigner crystal lattices in our dI/dV maps. The STM tip locally discharges the moiré electron localized at the AB_1 site closest to the tip apex once V_{bias} is large enough and the tip–electron distance is short enough. This enables discharge features centred around filled AB_1 sites to be observed in dI/dV maps of the graphene sensing layer.

In conclusion, our new STM imaging technique combines high spatial resolution and sensitivity with minimal perturbation and allows direct imaging of 2D generalized Wigner crystals in real space. This technique should be generally applicable to a wide variety of van der Waals moiré heterostructures and provides a powerful tool for imaging real-space electron configurations of novel correlated quantum phases in 2D systems.

Online content

Any methods, additional references, Nature Research reporting summaries, source data, extended data, supplementary information, acknowledgements, peer review information; details of author contributions and competing interests; and statements of data and code availability are available at <https://doi.org/10.1038/s41586-021-03874-9>.

1. Wigner, E. On the interaction of electrons in metals. *Phys. Rev.* **46**, 1002–1011 (1934).
2. Goldman, V., Santos, M., Shayegan, M. & Cunningham, J. Evidence for two-dimensional quantum Wigner crystal. *Phys. Rev. Lett.* **65**, 2189–2192 (1990).

3. Jang, J., Hunt, B. M., Pfeiffer, L. N., West, K. W. & Ashoori, R. C. Sharp tunnelling resonance from the vibrations of an electronic Wigner crystal. *Nat. Phys.* **13**, 340–344 (2017).
4. Zhou, H., Polshyn, H., Taniguchi, T., Watanabe, K. & Young, A. Solids of quantum Hall skyrmions in graphene. *Nat. Phys.* **16**, 154–158 (2020).
5. Shapir, I. et al. Imaging the electronic Wigner crystal in one dimension. *Science* **364**, 870–875 (2019).
6. Regan, E. C. et al. Mott and generalized Wigner crystal states in WSe_2/WS_2 moiré superlattices. *Nature* **579**, 359–363 (2020).
7. Jin, C. et al. Stripe phases in WSe_2/WS_2 moiré superlattices. *Nat. Mater.* **20**, 940–944 (2021).
8. Xu, Y. et al. Correlated insulating states at fractional fillings of moiré superlattices. *Nature* **587**, 214–218 (2020).
9. Huang, X. et al. Correlated insulating states at fractional fillings of the WS_2/WSe_2 moiré lattice. *Nat. Phys.* **17**, 715–719 (2021).
10. Deshpande, V. V. & Bockrath, M. The one-dimensional Wigner crystal in carbon nanotubes. *Nat. Phys.* **4**, 314–318 (2008).
11. Crandall, R. & Williams, R. Crystallization of electrons on the surface of liquid helium. *Phys. Lett. A* **34**, 404–405 (1971).
12. Williams, R., Crandall, R. & Willis, A. Surface states of electrons on liquid helium. *Phys. Rev. Lett.* **26**, 7–9 (1971).
13. Grimes, C. & Adams, G. Evidence for a liquid-to-crystal phase transition in a classical, two-dimensional sheet of electrons. *Phys. Rev. Lett.* **42**, 795–798 (1979).
14. Williams, F. Collective aspects of charged-particle systems at helium interfaces. *Surface Sci.* **113**, 371–388 (1982).
15. Lam, P. K. & Girvin, S. Liquid-solid transition and the fractional quantum-Hall effect. *Phys. Rev. B* **30**, 473–475 (1984).
16. Levesque, D., Weis, J. & MacDonald, A. Crystallization of the incompressible quantum-fluid state of a two-dimensional electron gas in a strong magnetic field. *Phys. Rev. B* **30**, 1056–1058 (1984).
17. Tsui, D. C., Stormer, H. L. & Gossard, A. C. Two-dimensional magnetotransport in the extreme quantum limit. *Phys. Rev. Lett.* **48**, 1559–1562 (1982).
18. Klitzing, K. V., Dorda, G. & Pepper, M. New method for high-accuracy determination of the fine-structure constant based on quantized Hall resistance. *Phys. Rev. Lett.* **45**, 494–497 (1980).
19. Pan, H., Wu, F. & Sarma, S. D. Quantum phase diagram of a moiré-Hubbard model. *Phys. Rev. B* **102**, 201104 (2020).
20. Hubbard, J. Generalized Wigner lattices in one dimension and some applications to tetracyanoquinodimethane (TCNQ) salts. *Phys. Rev. B* **17**, 494–505 (1978).
21. Li, H. et al. Imaging local discharge cascades for correlated electrons in WS_2/WSe_2 moiré superlattices. *Nat. Phys.* <https://doi.org/10.1038/s41567-021-01324-x> (2021).
22. Li, H. et al. Imaging moiré flat bands in three-dimensional reconstructed WSe_2/WS_2 superlattices. *Nat. Mater.* **20**, 945–950 (2021).
23. Zhang, Y. et al. Giant phonon-induced conductance in scanning tunnelling spectroscopy of gate-tunable graphene. *Nat. Phys.* **4**, 627–630 (2008).
24. Jung, S. et al. Evolution of microscopic localization in graphene in a magnetic field from scattering resonances to quantum dots. *Nat. Phys.* **7**, 245–251 (2011).
25. Decker, R. et al. Local electronic properties of graphene on a BN substrate via scanning tunnelling microscopy. *Nano Lett.* **11**, 2291–2295 (2011).
26. Wong, D. et al. Spatially resolving density-dependent screening around a single charged atom in graphene. *Phys. Rev. B* **95**, 205419 (2017).
27. Yang, F. et al. Experimental determination of the energy per particle in partially filled Landau levels. *Phys. Rev. Lett.* **126**, 156802 (2021).
28. Li, T. et al. Charge-order-enhanced capacitance in semiconductor moiré superlattices. *Nat. Nanotechnol.* <https://doi.org/10.1038/s41565-021-00955-8> (2021).
29. Tomarken, S. L. et al. Electronic compressibility of magic-angle graphene superlattices. *Phys. Rev. Lett.* **123**, 046601 (2019).
30. Zondiner, U. et al. Cascade of phase transitions and Dirac revivals in magic-angle graphene. *Nature* **582**, 203–208 (2020).
31. Pierce, A. T. et al. Unconventional sequence of correlated Chern insulators in magic-angle twisted bilayer graphene. Preprint at <https://arxiv.org/abs/2101.04123> (2021).
32. Pradhan, N. A., Liu, N., Silien, C. & Ho, W. Atomic scale conductance induced by single impurity charging. *Phys. Rev. Lett.* **94**, 076801 (2005).
33. Brar, V. W. et al. Gate-controlled ionization and screening of cobalt adatoms on a graphene surface. *Nat. Phys.* **7**, 43–47 (2011).
34. Wong, D. et al. Characterization and manipulation of individual defects in insulating hexagonal boron nitride using scanning tunnelling microscopy. *Nat. Nanotechnol.* **10**, 949–953 (2015).
35. Teichmann, K. et al. Controlled charge switching on a single donor with a scanning tunnelling microscope. *Phys. Rev. Lett.* **101**, 076103 (2008).

Publisher's note Springer Nature remains neutral with regard to jurisdictional claims in published maps and institutional affiliations.

© The Author(s), under exclusive licence to Springer Nature Limited 2021

Methods

Sample fabrication

The encapsulated WSe₂/WS₂ moiré heterostructure stack was fabricated using the micro-mechanical stacking technique³⁶. A poly(propylene) carbonate (PPC) film stamp was used to pick up all exfoliated 2D material flakes. The 2D material layers in the main heterostructure region were picked up in the following order: bottom hBN, WSe₂, WS₂, top hBN and then monolayer graphene. A graphite layer was also picked up between the WS₂ and the top hBN to serve as a contact electrode of the WSe₂/WS₂ heterostructure. The PPC film together with the stacked sample was then peeled, flipped over and transferred onto a Si/SiO₂ substrate (SiO₂ thickness 285 nm). The PPC layer was subsequently removed using ultrahigh vacuum annealing at 230 °C, resulting in an atomically clean heterostructure suitable for STM measurements. A 50 nm Au and 5 nm Cr metal layer was then evaporated through a shadow mask to form the electric contact.

STM and scanning tunnelling spectroscopy measurement

STM and scanning tunnelling spectroscopy (STS) measurements were performed using a Pt/Ir etched tip at temperature $T = 5.4$ K and pressure $= 2 \times 10^{-10}$ torr. The STS (d/dV spectra and mapping) were performed with a tip bias modulation of 15 mV amplitude and approximately 500–900 Hz frequency. The d/dV mapping of the Mott-insulator state in Fig. 2c was performed under open-loop conditions with the tip height set by the following parameters: $V_{\text{bias}} = 180$ mV and $I = 300$ pA. d/dV mappings of the generalized Wigner crystals states were performed under constant-current mode if not further specified.

WSe₂/WS₂ twist angle calculation

The measured moiré lattice constant is $L_M = 8$ nm, yielding the twist angle between the WSe₂ and WS₂ layers $\theta \approx 0^\circ$ through the formula $L_M = \frac{a}{\sqrt{\delta^2 + \theta^2}}$, where $\delta = (a - a')/a$ is the lattice mismatch, $a = 3.153$ Å and $a' = 3.28$ Å are the atomic lattice constants of the WS₂ and WSe₂, respectively³⁷.

Individual d/dV spectra

Extended Data Figure 1a displays the evolution of the d/dV spectra for $V_{\text{TG}} = 0$ and different values of V_{BG} . We observe that the Dirac point (characterized by a dip in the local DOS and marked by grey arrows) shifts from positive bias to negative bias voltage with increased V_{BG} , corresponding to a change from the graphene hole-doped regime to the graphene electron-doped regime. The small tunnelling current close to zero bias voltage is due to reduced tunnelling from graphene electrons at the K and K' points of the graphene band structure²³ (phonon-induced inelastic tunnelling additionally causes rises in tunnel current that can result in gap-like features in graphene d/dV spectra²³).

Extended Data Figure 1b displays the d/dV spectra at $V_{\text{TG}} = 0.53$ V for different V_{BG} . The WS₂/WSe₂ moiré heterostructure is conducting at $V_{\text{BG}} = 6$ V, 25 V and 37 V. The d/dV spectra for these back-gate voltages remain almost constant and correspond to charge neutral or a weak hole doping. These spectra are comparable to the spectrum at $V_{\text{BG}} = -6$ V for $V_{\text{TG}} = 0$ V (shown in Extended Data Fig. 1a). The d/dV spectra change obviously at $V_{\text{BG}} = 12$ V, 16.1 V, 19.5 V and 30.5 V, which correspond to the Wigner crystal and Mott insulator states at $n = 1/3, 1/2, 2/3$ and 1. These spectra are characteristic of electron-doped graphene. They are comparable to the spectra at $V_{\text{BG}} = -2$ V and 0 V for $V_{\text{TG}} = 0$ (shown in Extended Data Fig. 1a). This indicates that the back gate can induce finite electron doping in the graphene when the WS₂/WSe₂ moiré heterostructure is in a correlated insulating state due to the electron incompressibility of the correlated insulators.

Moiré site dependence of the d/dV spectra

Extended Data Figure 2a shows the topography of the moiré superlattice. Extended Data Figure 2b–d shows the graphene d/dV spectra along the

AA–AB₁–AB₂–AA line in Extended Data Fig. 2a for $V_{\text{TG}} = 0.7$ V and $V_{\text{BG}} = 19$ V, 26.5 V, 35 V, respectively. We find that the graphene d/dV spectra are very similar at all positions. The doped WS₂/WSe₂ moiré heterostructure (and the Wigner crystal states) mostly shifts the average electron doping in the graphene monolayer. The spatial dependence is weak and only observable over narrow bias voltage ranges associated with the discharging of moiré electrons (as shown in Figs. 2 and 3 of the main text.)

We can understand this effect by noting that the doped moiré heterostructure provides only a relatively small modulation of the potential energy in graphene. Electrons in monolayer graphene are described by relativistic Dirac electrons which tend to be highly delocalized close to the CNP. The screening length of Dirac electrons diverges at the CNP and is longer than 8 nm for doping level below 1×10^{11} cm⁻² (see ref. ²⁶). As a result, electron density modulation (and associated d/dV changes) at the moiré period scale is very small in charge neutral monolayer graphene.

Raw images and FFT filtering of the generalized Wigner crystal states

The d/dV images of the generalized Wigner crystal states shown in Fig. 2 of the main text are FFT filtered to suppress the periodic feature associated with the moiré superlattice. Extended Data Figure 3 shows the unfiltered raw images of the generalized Wigner crystal states and the process of the FFT filtering.

Extended Data Figure 3a displays the raw d/dV map of the $n = 2/3$ state, with the corresponding FFT image shown in Extended Data Fig. 3b. Here the red circles label the positions of reciprocal unit vectors of the moiré superlattice. We filter out the signal within the red circles in the FFT filtering process. Extended Data Fig. 3c shows the FFT filtered image of Extended Data Fig. 3a (same as Fig. 2e in the main text) and Extended Data Fig. 3d shows the corresponding filtered FFT image (same as Fig. 2f in the main text).

Similar filtering procedures are performed for the $n = 1/3$ and $n = 1/2$ Wigner crystal states. Extended Data Fig. 3e, f show the raw real space and FFT images, respectively, of the $n = 1/3$ Wigner crystal state, and the corresponding FFT filtered images are shown in Extended Data Fig. 3g, h. Extended Data Fig. 3i, j show the raw real space and FFT images, respectively, of the $n = 1/2$ Wigner crystal state, and the corresponding FFT filtered images are shown in Extended Data Fig. 3k, l.

Discussion on the $n = 1/2$ Wigner crystal state

The broken symmetry of the $n = 1/2$ state could be impacted by accidental strain in the lattice, since stripes extending in the stretched lattice direction can have lower energy. We can characterize the sample anisotropy in the topography image shown in Fig. 1b (reproduced in Extended Data Fig. 4a). The corresponding FFT image is shown in Extended Data Fig. 4b. Both the moiré lattice (in real space) and the diffraction pattern (in reciprocal space) show a small deviation from perfect honeycomb lattice. To better illustrate the anisotropy in the moiré lattice, Extended Data Fig. 4c shows a one-dimensional topography plot along the red lines in Extended Data Fig. 4a. The corresponding FFT results are shown in Extended Data Fig. 4d. The moiré periods along the three different directions are slightly different, from which we can estimate a uniaxial strain of 0.39% following the model described in reference³⁸. The pink double arrowed line in Extended Data Fig. 4a, b shows the direction of the extensive uniaxial strain. For comparison, the stripe direction of the $n = 1/2$ state is also denoted by the yellow double arrowed line in Extended Data Fig. 4a, b. We find that the stripe direction is close to the uniaxial strain direction, suggesting a correlation between the strain and the broken symmetry of the stripe phase.

Experimentally we also find that the $n = 1/2$ state is more fragile than the $n = 1/3$ and $n = 2/3$ states. A well-defined generalized Wigner crystal stripe phase is present only in a very narrow parameter space of V_{bias} and V_{BG} . The $n = 1/2$ state is also more sensitive to local inhomogeneity, as reflected by the disordering of the stripe electron lattice near the right

Article

edge of the image in Fig. 2i as compared to the more defect-free $n = 2/3$ (Fig. 2c) and $n = 1/3$ (Fig. 2e) states. Further studies of the generalized Wigner crystal electron lattice at $n = 1/2$ could potentially lead to a better understanding of the competition of different quantum phases controlled by long-range Coulomb interactions.

Data availability

The data supporting the findings of this study can be found at https://github.com/HongyuanLiCMP/Imaging_Generalized_Wigner_Crystals_data, and are also available from the corresponding authors upon reasonable request.

36. Wang, L. et al. One-dimensional electrical contact to a two-dimensional material. *Science* **342**, 614–617 (2013).
37. Schutte, W., De Boer, J. & Jellinek, F. Crystal structures of tungsten disulfide and diselenide. *J. Solid State Chem.* **70**, 207–209 (1987).
38. Kerelsky, A. et al. Maximized electron interactions at the magic angle in twisted bilayer graphene. *Nature* **572**, 95–100 (2019).

Acknowledgements This work was primarily funded by the US Department of Energy, Office of Science, Office of Basic Energy Sciences, Materials Sciences and Engineering Division

under contract no. DE-AC02-05-CH11231 (van der Waals heterostructure program KCFW16) (device electrode preparation and STM spectroscopy). Support was also provided by the US Army Research Office under MURI award W911NF-17-1-0312 (device layer transfer), and by the National Science Foundation Award DMR-1807233 (surface preparation). S.T. acknowledges support from DOE-SC0020653, NSF DMR 2111812, NSF DMR 1552220, NSF 2052527, DMR 1904716 and NSF CMMI 1933214 for WSe₂ and WS₂ bulk crystal growth and analysis. K.W. and T.T. acknowledge support from the Elemental Strategy Initiative conducted by the MEXT, Japan, grant number JPMXP0112101001, JSPS KAKENHI grant number JP20H00354 and the CREST(JPMJCR15F3), JST for bulk hBN crystal growth and analysis. E.C.R. acknowledges support from the Department of Defense (DoD) through the National Defense Science and Engineering Graduate Fellowship (NDSEG) Program. S.L. acknowledges support from Kavli ENSI Heising Simons Junior Fellowship. We also thank M. H. Naik for sharing unpublished theoretical simulation data on the WSe₂/WS₂ moiré superlattice.

Author contributions M.F.C. and F.W. conceived the project. H.L. and S.L. performed the STM measurement. H.L., E.C.R., D.W., W.Z. and S.K. fabricated the heterostructure device and performed the SHG measurement. K.Y., M.B. and S.T. grew WSe₂ and WS₂ crystals. K.W. and T.T. grew the hBN single crystal. All authors discussed the results and wrote the manuscript.

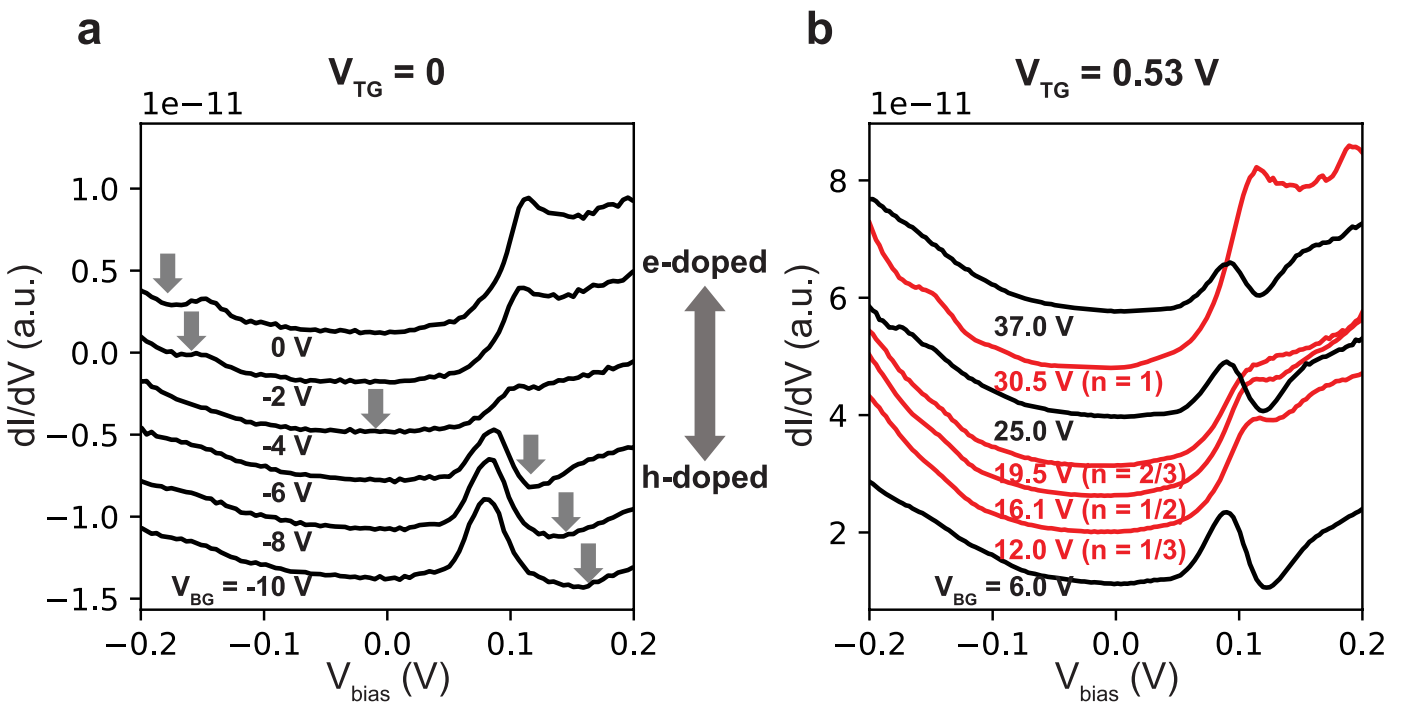
Competing interests The authors declare no competing interests.

Additional information

Correspondence and requests for materials should be addressed to S.L., M.F.C. or F.W.

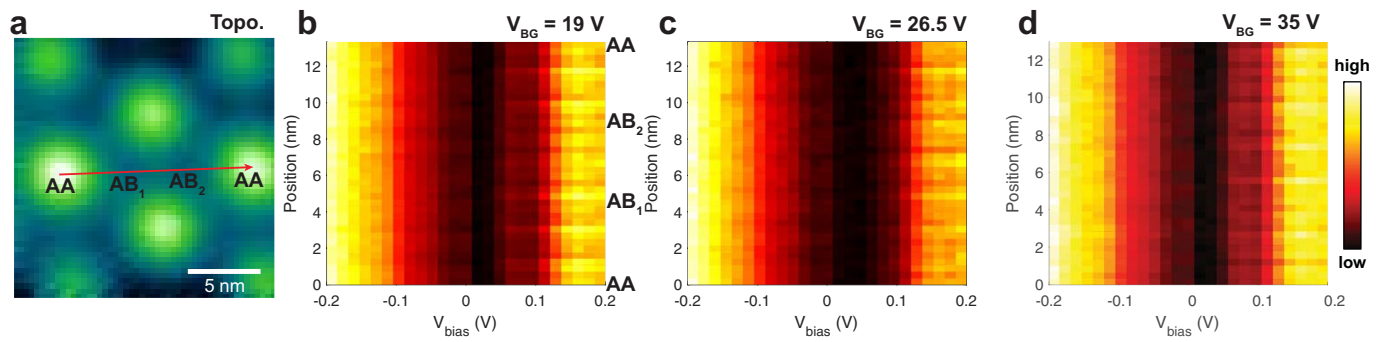
Peer review information *Nature* thanks the anonymous reviewers for their contribution to the peer review of this work.

Reprints and permissions information is available at <http://www.nature.com/reprints>.

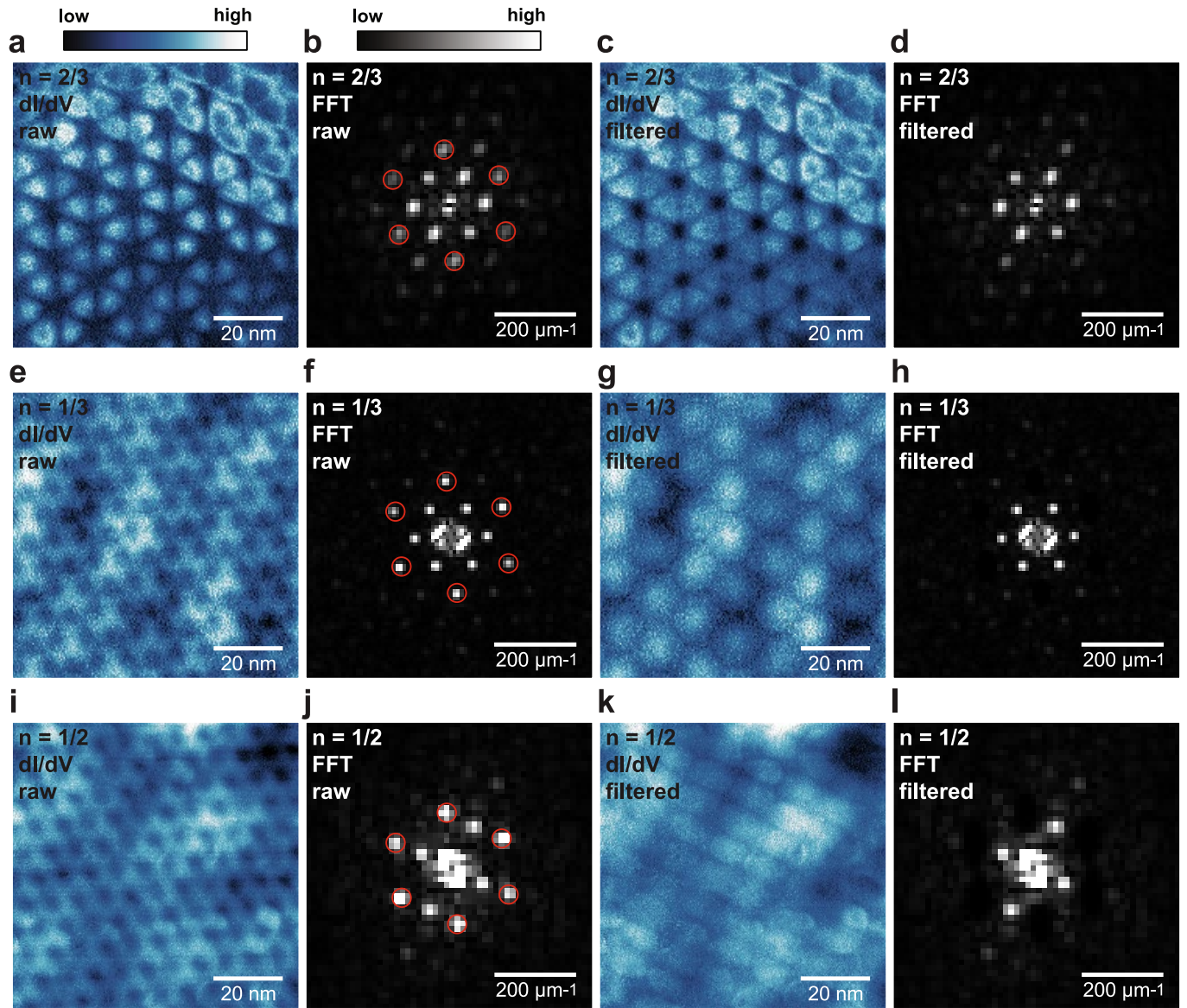


Extended Data Fig. 1 | Comparison of single dI/dV spectra obtained at $V_{TG} = 0$ and $V_{TG} = 0.53$ V. **a**, $V_{TG} = 0$. **b**, $V_{TG} = 0.53$ V. In **a** we display dI/dV spectra obtained when the graphene doping is near the CNP. A strong spectral change is observed when the graphene transitions from hole-doped to electron-doped. The Dirac point positions are denoted by vertical arrows.

In **b** we display typical dI/dV spectra at $n = 1/3, 1/2, 2/3$ and 1 for correlated states (red) as well as for three other filling factors that lack correlated states (black). In each panel the dI/dV spectra are shifted vertically for clarity. The spectra indicate that the graphene sensing layer is more electron doped when the moiré heterostructure is in a correlated insulator state.

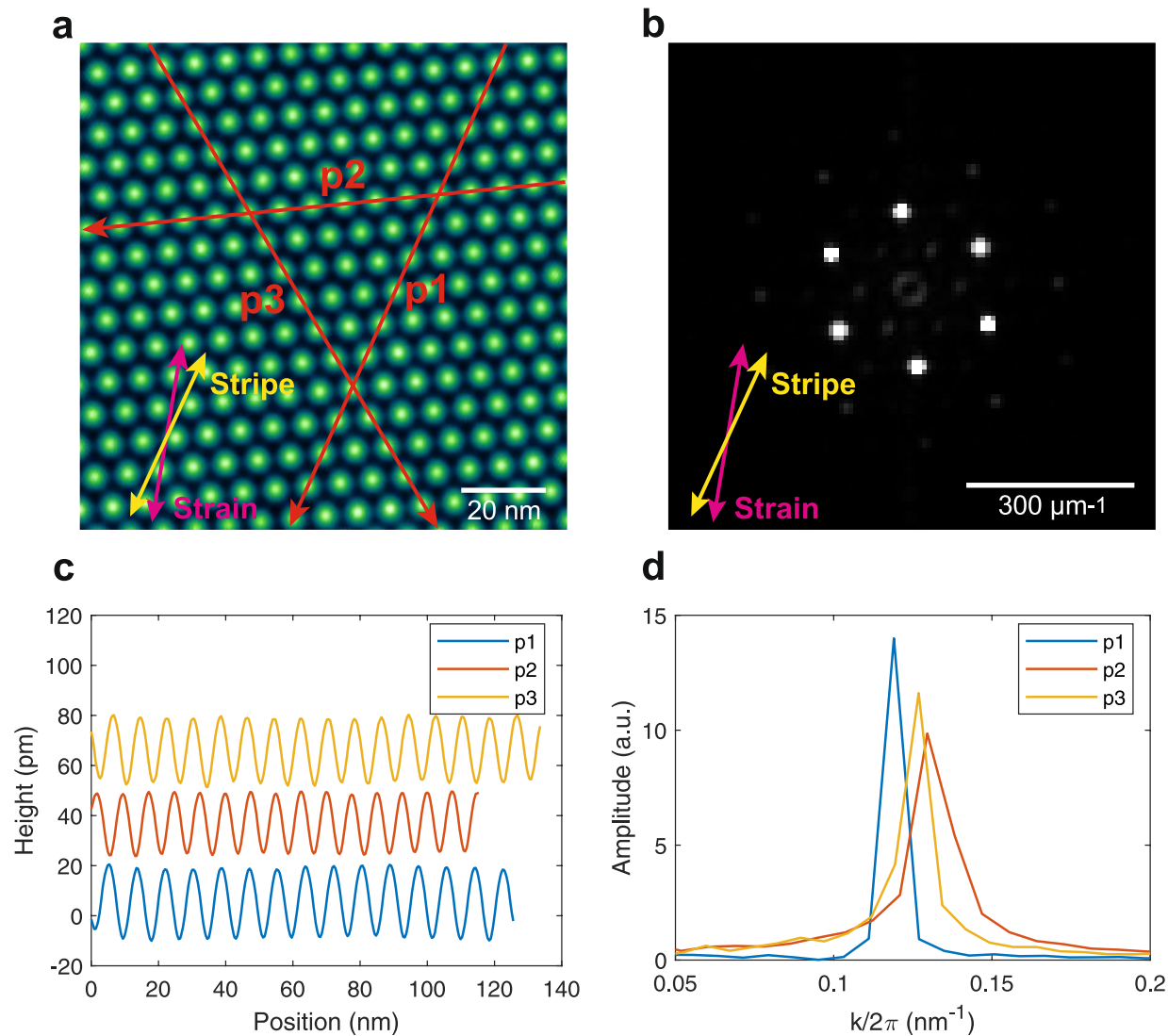


Extended Data Fig. 2 | Moiré site dependence of the dI/dV spectra. **a**, A typical STM topographic image of the moiré superlattice seen through the graphene sensing layer. **b–d**, Position dependent dI/dV spectra measured along the red linecut shown in **a** with $V_{TG} = 0.7$ V and $V_{BG} = 19$ V (**b**), 26.5 V and 35 V (**d**).



Extended Data Fig. 3 | Raw images and FFT filtering of the dI/dV maps for the generalized Wigner crystal states. **a**, Raw dI/dV map of the $n = 2/3$ state. **b**, FFT image of **a**. **c**, Real space dI/dV map after FFT filtering of **a**. In the filtering process, we removed the Fourier components within the six red circles indicated in **b**. This FFT filtering suppresses the periodic feature associated with the moiré superlattice. **d**, FFT image of **c**. **e**, Raw dI/dV map of the $n = 1/3$

state. **f**, FFT image of **e**. **g**, Real space dI/dV map after FFT filtering of **e**. The Fourier components within the red circles shown in **f** have been filtered out. **h**, FFT image of **g**. **i**, Raw dI/dV map of the $n = 1/2$ state. **j**, FFT image of **i**. **k**, Real-space dI/dV map after FFT filtering of **i**. The Fourier components within the red circles shown in **j** have been filtered out. **l**, FFT image of **k**.



Extended Data Fig. 4 | Uniaxial strain of the moiré superlattice.

a, Topography image shown in Fig. 1b. **b**, the corresponding FFT image. **c, d**, 1D height modulation along three directions (**c**; denoted by the red arrows in **a**), and the corresponding FFT results (**d**). The different moiré periods along

the three different directions yields a uniaxial strain of 0.39% along the pink double-arrowed line (**a, b**). As a comparison, the stripe direction of the $n = 1/2$ Wigner crystal state is denoted by the yellow double-arrowed line.